The Astrophysical Journal, 926:17 (16pp), 2022 February 10 https://doi.org/10.3847/1538-4357/ac3a72
© 2022. The Author(s). Published by the American Astronomical Society.
OPEN ACCESS

Anomalous Orbital Characteristics of the AQ Col (EC 05217-3914) System

T. Otani[1], A. E. Lynas-Gray[2,3,4], D. Kilkenny[4], C. Koen[5], T. von Hippel[1], M. Uzundag[6,7], M. Vučković[6], C. M. Pennock[8], and R. Silvotti[9]
[1] Department of Physical Sciences and SARA, Embry-Riddle Aeronautical University, 1 Aerospace Boulevard, Daytona Beach, FL 32114, USA; otanit@erau.edu
[2] Department of Physics and Astronomy, University College London, Gower Street, London WC1E 6BT, UK
[3] Department of Physics, University of Oxford, Keble Road, Oxford OX1 3RH, UK
[4] Department of Physics and Astronomy, University of the Western Cape, Bellville 7535, South Africa
[5] Department of Statistics, University of the Western Cape, Bellville 7535, South Africa
[6] Instituto de Física y Astronomía, Universidad de Valparaíso, Gran Bretaña 1111, Playa Ancha, Valparaíso, 2360102, Chile
[7] European Southern Observatory, Alonso de Cordova 3107, Santiago, Chile
[8] Lennard-Jones Laboratories, Keele University, ST5 5BG, UK
[9] INAF-Osservatorio Astrofisico di Torino, strada dell'Osservatorio 20, 10025 Pino Torinese, Italy
Received 2021 September 6; revised 2021 November 14; accepted 2021 November 15; published 2022 February 8

Abstract

AQ Col (EC 05217-3914) is one of the first detected pulsating subdwarf B (sdB) stars and has been considered to be a single star. Photometric monitoring of AQ Col reveals a pulsation timing variation with a period of 486 days, interpreted as time delay due to reflex motion in a wide binary formed with an unseen companion with expected mass larger than 1.05 $M_{\odot}$. The optical spectra and color–magnitude diagram of the system suggested that the companion is not a main-sequence star but a white dwarf or neutron star. The pulsation timing variation also shows that the system has an eccentricity of 0.424, which is much larger than any known sdB long period binary system. That might be due to the existence of another short period companion to the sdB star. Two optical spectra obtained on 1996 December 5 show a radial velocity change of 49.1 km s^{-1} in 46.1 minutes, which suggests the hot subdwarf in the wide binary is itself a close binary formed with another unseen white dwarf or neutron star companion; if further observations show this interpretation to be correct, AQ Col is an interesting triple system worthy of further study.

Unified Astronomy Thesaurus concepts: Multiple stars (1081); Variable stars (1761); Subdwarf stars (2054); Extreme horizontal branch stars (513); Stellar evolution (1599); Timing variation methods (1703); Pulsation frequency method (1308); White dwarf stars (1799)

Supporting material: data behind figure, figure set, machine-readable table

1. Introduction

Subdwarf B (sdB) stars are core helium-burning objects, found in both the disk and halo of our galaxy (Saffer et al. 1994). EC 14026-2647 (=V361 Hya) was the first pulsating sdB star to be discovered (Kilkenny et al. 1997), possibly because, as suggested by Østensen et al. (2010), only about 10% of these pressure mode (p-mode) sdB stars have pulsations detectable from the ground. The observed properties of sdB stars place them on the extreme horizontal branch (EHB). Their effective temperatures range from 22,000–40,000 K and surface gravities range from $5.0 \leqslant \log g \leqslant 6.2$ (in cgs units). Their masses are narrowly confined to about 0.5 $M_{\odot}$ (Heber 2009). sdB stars have experienced mass loss at, or just before the end of the red giant branch phase (Bonanno et al. 2003), in which the hydrogen envelope is lost, leaving a helium core with a very thin inert hydrogen-rich envelope. The loss of the hydrogen envelope prevents the stars from entering the red clump phase and subsequently ascending the asymptotic giant branch; instead, and they settle on the EHB, spending about 10^8 yr as sdB stars. Upon helium depletion in the core they become subdwarf O (sdO) stars burning helium in a shell surrounding a C/O core, and eventually, DAO white dwarfs (Dorman et al. 1993; Bergeron et al. 1994).

Original content from this work may be used under the terms of the Creative Commons Attribution 4.0 licence. Any further distribution of this work must maintain attribution to the author(s) and the title of the work, journal citation and DOI.

Plausible sdB formation models via binary evolution were constructed by Han et al. (2002, 2003) and more than 50% of hot subdwarfs are understood to be members of binary systems (see, e.g., Silvotti et al. (2018) and references therein). However, some fraction of sdB stars may not be in binaries (Heber 2009; Fontaine et al. 2012). If true, this would require another formation channel, perhaps the single star evolution scenario proposed by both Dorman et al. (1993) and D'Cruz et al. (1996). In another scenario, the merger of a helium white dwarf with a low-mass hydrogen-burning star was proposed as a way of forming single sdB stars (Clausen & Wade 2011). Wu et al. (2018, 2020) recently suggested the possibility that sdB + neutron star (NS) binary systems should contribute 0.3%–0.5% of the total sdB binaries. To distinguish between these evolutionary scenarios, orbital information on sdB star binaries is essential.

The existence of sdB pulsators (sdBV, where the "V" stands for variable), adopting the classification scheme Kilkenny (2010) proposed, was predicted by Charpinet et al. (1996). Independently, Kilkenny et al. (1997) discovered the first short period sdBV star, EC 14026-2647. These stars are p-mode pulsators, where pulsations are driven by internal pressure fluctuations (Charpinet et al. 2000). The first long period sdBV star, PG 1716+426, is a g-mode pulsator (Green et al. 2003), in which gravity provides the restoring force. Some sdB stars have been discovered to exhibit both p-mode and g-mode pulsations. These objects are called hybrid pulsators (Oreiro et al. 2004; Schuh et al. 2006).

Although amplitudes often vary (e.g., Kilkenny 2010), the pulsation periods of sdBV stars are usually stable (Østensen et al. 2001), and therefore they are good chronometers. As is well known, a star's position in space may show cyclic variations due to the gravitational perturbations of a companion. From an observer's point of view, the light from the pulsating star is periodically delayed when it is on the far side of its orbit and advanced on the near side. The orbital solution of the binary system can be obtained from changes in the pulsation arrival times, and this is referred to as the pulsation timing method. This technique has long been used in the binary star community to search for additional components, orbital period changes, mass loss, etc.

Several candidate planets and companions to sdB host stars have been detected by this method. Silvotti et al. (2007, 2018) detected a planet candidate around the sdB star V391 Peg in this way. Lutz (2011) detected companions to the sdB stars HS 0444+458 and HS 0702+6043, which appear to be a brown dwarf and an exoplanet, respectively. However, Mackebrandt et al. (2020) did not confirm these tentative determinations. Mullally et al. (2008) used this Observed minus Calculated (O–C) method to search for possible planets around DAV white dwarfs. Among the 15 white dwarf stars they surveyed, GD 66 exhibited O–C variations consistent with a 2 M_J planet in a 4.5 yr orbit, which, however, was not confirmed by Dalessio (2013). Zong et al. (2016, 2018) recently pointed out that the pulsation frequencies of sdB stars and white dwarfs show variations and that require us to be more cautious in using the pulsation timing method to search for small mass objects like planets. However, this method is still an efficient tool to obtain an orbital solution of a binary system. The presence of M-dwarf or white dwarf companion to the sdBV star CS 1246, suggested by O–C variations, was confirmed by radial velocity (RV) measurements (Barlow et al. 2011a, 2011b). Similarly, Otani et al. (2018) used this method to obtain an orbital solution of the previously known sdB and main-sequence binary, EC 20117-4014. It is perhaps worth noting here that Bours et al. (2016) present O–C diagrams for more than 50 white dwarf binaries and suggest that the period variations might be due to magnetic effects (such as the Applegate mechanism; Applegate 1992) in the cool companions. However, where there are substantial baselines, these binaries do not show repeatable cyclic variations and the timescales of the effects are much longer than those described here.

AQ Col (EC 05217-3914) is an sdB star originally found in the Edinburgh-Cape (EC) Blue Object Survey (Stobie et al. 1997; Kilkenny et al. 2016). The spectra obtained by Koen et al. (1999) did not suggest that AQ Col has a companion. The apparent magnitude of the star is $V = 15.55$ (Koen et al. 1999). Three pulsation periods of 218, 216, and 213 s were detected, making AQ Col one of the first members of the class of short period sdBV stars. Further high speed photometry of AQ Col was obtained and an asteroseismic analysis was performed by Billères & Fontaine (2005), who estimated the effective temperature ($T_{\rm eff} = 32{,}000$ K), gravity ($\log g = 5.730$), and mass ($M_* = 0.49\ M_\odot$). They also found two additional pulsation periods at 208 and 129 s.

Although AQ Col has been believed to be a single sdB star for decades, our pulsation timing analysis using the three largest amplitude pulsations show periodic variations, which indicate that AQ Col has a companion with a long orbital period. So far, we have photometric data spread over nearly 25 yr for AQ Col. In this paper, we present the results of our pulsation timing analysis, and the extracted orbital information for the system. We also analyzed the spectroscopic data of Koen et al. (1999) and an additional spectrum obtained in 2020. The RV differences obtained from the spectroscopic data indicate that AQ Col may have another companion with a short orbital period, which we also discuss.

Section 2 outlines the facilities and instrumentation used to obtain the data needed for the analysis and our reduction procedures. Section 3 shows the pulsation timing method that we used. Section 4 presents our results derived from the observed pulsation peaks in the frequency spectrum of AQ Col and spectroscopy data. Our conclusions and suggested additional work are summarized in Section 5.

2. Observations and Data Reduction

2.1. Photometry Data

The observation log is presented in Table 1. For observations made at the Southeastern Association for Research in Astronomy at Cerro Tololo Inter-American Observatory, Chile (SARA-CT), no filter has been used since the target was faint for the 0.6 m SARA-CT telescope[10] (Keel et al. 2017). To reduce read-out noise, 3 × 3 on-chip binning was used for the images. The exposure time was 30 s until 2018 Feb 2 but reduced to 15 s after 2018 Feb 26. The pulsations frequencies and amplitudes are expected to be wavelength dependent (see Koen (1998)). However, separate analyses were performed using only the South African Astronomical Observatory (SAAO) data, and both SAAO and SARA-CT data to compare the results. The pulsation timing analysis results with and without the SARA-CT data were the same within the uncertainty. Therefore, the results presented in this paper include the data taken with SARA-CT.

For the calibration and reduction of SARA-CT data, standard procedures were performed using AstroImageJ (Collins et al. 2017)[11]. All flat fields were exposed in a twilight sky. For each night's data, the aperture that gave the best signal-to-noise ratio (S/N) was chosen and sky annuli were used to subtract the sky background. These values were then divided by similarly extracted intensity values of nonvariable comparison stars.

The early data in Table 1 were obtained using a mixture of the SAAO 1 m telescope with a photomultiplier-based photometer, or the SAAO 0.75 m and 1 m telescopes with the UCT CCD photometer (see Koen et al. 1999). All later observations were made with the SAAO 1 m telescope with different charge-coupled device (CCD) photometers—between 2006 and mid-2012 using the UCT CCD; between mid-2012 and 2019 using the SAAO STE3 CCD; and post-2019, the STE4 CCD—the undesirable change of CCDs being forced by the demise of the earlier instruments. The photomultiplier data were reduced by subtracting a cubic-spline fit to occasional sky measurements from each star measurement and then correcting for atmospheric extinction (see O'Donoghue et al. (1997) for details). The CCD data were reduced using an automated version of the DoPhot software (Schechter et al. 1993). A detailed description of both the UCT CCD and the CCD reduction process is given in O'Donoghue et al. (1996) and information on the STE3 and STE4 photometers can be found on the SAAO web page[12].

[10] SARA-CT 0.6 m telescope is owned and operated by the Southeastern Association for Research in Astronomy (saraobservatory.org).
[11] https://www.astro.louisville.edu/software/astroimagej
[12] www.saao.ac.za/astronomers/ste3-ste4/

Table 1
Observation Log for AQ Col

Date	Mean Time (BJD−2453500)	Observation Length (min)	Observatory
1996 Jan 28	−3388.60	252.2	SAAO
1996 Feb 17	−3368.63	217.2	SAAO
1996 Dec 5	−3076.56	460.4	SAAO
1996 Dec 9	−3072.57	422.5	SAAO
1998 Jan 27	−2658.59	304.4	SAAO
1998 Jan 28	−2657.59	302.2	SAAO
1998 Feb 1	−2653.61	329.1	SAAO
2006 Dec 19	589.38	264.1	SAAO
2007 Feb 18	650.33	164.5	SAAO
2010 Oct 15	1984.79	242.4	SARA-S
2010 Dec 9	2039.70	389.2	SARA-S
2010 Dec 10	2040.69	420.0	SARA-S
2015 Nov 7	3833.74	319.4	SARA-S
2015 Dec 8	3864.69	438.9	SARA-S
2016 Feb 7	3925.70	151.5	SARA-S
2017 Oct 17	4544.56	188.0	SAAO
2017 Oct 20	4546.52	86.8	SAAO
2017 Oct 21	4547.55	192.4	SAAO
2018 Jan 15	4633.72	157.0	SARA-S
2018 Jan 19	4637.64	210.2	SARA-S
2018 Feb 2	4651.61	178.1	SARA-S
2018 Feb 26	4675.61	159.9	SARA-S
2018 Mar 14	4692.29	134.5	SAAO
2018 Mar 16	4694.28	116.0	SAAO
2018 Mar 17	4695.29	138.1	SAAO
2018 Mar 19	4697.28	114.0	SAAO
2018 Nov 8	4930.55	152.4	SAAO
2018 Nov 9	4931.51	159.2	SAAO
2018 Nov 10	4932.55	128.6	SAAO
2018 Nov 12	4934.53	223.2	SAAO
2019 Jan 16	4999.70	316.6	SARA-S
2019 Feb 6	5021.34	183.7	SAAO
2019 Mar 6	5049.31	165.9	SAAO
2019 Mar 12	5055.30	148.4	SAAO
2019 Oct 29	5055.30	155.2	SAAO
2019 Nov 20	5308.51	136.5	SAAO
2019 Nov 22	5310.46	162.5	SAAO
2019 Nov 23	5311.50	234.5	SAAO
2019 Nov 24	5312.48	170.9	SAAO
2019 Nov 26	5314.51	213.9	SAAO
2020 Mar 13	5422.30	119.5	SAAO
2020 Mar 21	5430.28	124.3	SAAO

Notes. Only the observation dates in which the data show any pulsation amplitude $\geqslant 2\sigma$ above the noise level are shown. The 1996 and 1998 data were previously published in Koen et al. (1999).

For each night, the raw light curves were then normalized to the mean magnitude for that night. A quadratic curve was used to remove mild curvature in the light curves caused by differential extinction between the target and comparison stars. All times were corrected to Barycentric Julian Date (BJD) in Barycentric Dynamical Time (Eastman et al. 2010).

The normalized light curves were then analyzed using Period04 (Lenz 2004). To improve detection and characterization of the pulsation frequencies and amplitudes, the data were pre-whitened (Blackman & Tukey 1958). After one or more frequencies were identified in the amplitude spectrum, they were removed from each light curve by subtracting the corresponding least-squares fitted sine curve (Sullivan et al. 2008). This analysis was performed for each of the runs listed in Table 1. As described in Section 4, we only use peaks above 4σ for our analysis to find an orbital solution.

Table 2
Spectra Available for Analysis

Observation Date	Telescope	HJD 2440000 (mid-exposure)	RV (km s^{-1})
1989 December 21	SAAO 1.9 m	07881.52318	−89.2
1996 December 05	SAAO 1.9 m	10422.53204	+169.4
1996 December 05	SAAO 1.9 m	10422.56408	+120.3
2020 February 28	SOAR 4.1 m	18907.55403	+199.8

2.2. Spectroscopic Data

Spectra were obtained with the SAAO 1.9 m telescope as part of the EC Survey as Stobie et al. (1997) describe. As was standard practice for early EC Survey spectroscopy, a Reticon spectrograph (Jorden et al. 1982) was used with Grating-6 and a 250 μ slit, corresponding to 1.″8 and giving an effective resolution of FWHM $\simeq$ 3.5 Å. As was customary, a 100 s Cu/Ar arc spectrum was obtained before and after each sequence: star and sky spectra were obtained using separated detectors with an exposure time of 1200 s, and their role reversed for a second 1200 s exposure, with a third arc spectrum obtained between the two. A single wavelength-calibrated AQ Col spectrum corrected for sky background was thereby obtained, having a useful wavelength range of $3600 < \lambda < 5200$ Å. Spectra available for analysis are listed in Table 2, the sequence described above being used to secure all three SAAO spectra.

An additional spectrum ($3700 < \lambda < 7200$ Å) was observed with the Southern Astrophysical Research (SOAR) Telescope using the Goodman Spectrograph (Clemens et al. 2004); in this case the effective resolution was FWHM $\simeq$ 2.0Å. Barycentric RVs included in Table 2 were obtained by cross-correlating against a synthetic spectrum for the Koen et al. (1999) atmospheric parameters $T_{\rm eff} = 31{,}000$ K, $\log g = 5.7$, and $\log(N({\rm He})/N({\rm H})) = -5.0$, taken from the Németh et al. (2014) non-LTE grid; the $\log(N({\rm He})/N({\rm H}))$ choice being based on the absence of He I lines. Barycentric corrections were obtained following Wright & Eastman (2014).

3. Pulsation Timing Method

Stable light-curve variations shown by pulsations or eclipses can act as accurate clocks, and monitoring those timings allows us to search for phenomena such as the existence of planets and companions, stellar evolution, or apsidal motion of the binary system. This is one of the classic techniques in astronomy, and this principle was used by Rømer in the late 17th century to observe apparent periodic changes in Jupiter's Galilean moons and thus to estimate the speed of light.

To monitor timing variations in the light-curve oscillations, the O–C method is the most common method. Computing the time difference between an observed event and that calculated from an ephemeris allows one to determine an accurate period of the periodic event and to search for cyclic and secular variations. As is standard practice, the observed times of the light-curve maxima are used to form the ephemeris and then the O–C values are plotted as a function of time. Good reviews of this method can be found in Paparo et al. (1988), Sterken (2005), and Winget & Kepler (2008). The traditional O–C method uses the light-curve maxima to obtain the timing

variations; however, monitoring pulsation phase changes will also let one calculate the same timing variations (Murphy et al. 2014). This approach is called the phase modulation (PM) method and is particularly suited for analysis of multimode pulsators; it also allows us to obtain a better quality for the timing variations because all the data are used. Since AQ Col is a multimode pulsator, the PM method was used in this paper. However, the basic concept (obtaining the timing variations) and how to interpret the variations to the astronomical phenomenon are the same for both the O–C method and the PM method.

The pulsation timing variations, τ, can be expressed as a quadratic:

$$\tau = \frac{1}{2}P\dot{P}E^2 + \Delta P\, E + \Delta E_0, \tag{1}$$

where E is the integer counter of completed cycles after the first observation, P is the initially estimated period of pulsation, ΔE_0 is the difference between the observed and calculated reference epochs, ΔP is the difference between the actual period and the estimated period, and $\dot{P} = dP/dt$ (see Sterken 2005 and Winget & Kepler 2008 for details). The pulsation timing variations (this concept also works for the other timing methods such as the eclipse timing method) will be constant if no pulsation period changes are occurring and the assumed pulsation period is correct. If the calculated period is constant but incorrect, τ will be linear with a positive or negative slope. If the period is changing linearly with time (e.g., due to the star evolving or magnetic braking), τ will exhibit a quadratic form. The precision of this technique, when applied to observations spanning several years, has allowed empirical measurement of the cooling rates of white dwarf stars and the evolution of sdB stars (Kepler et al. 1991; Silvotti et al. 2007; Costa & Kepler 2008; Winget & Kepler 2008; Lutz 2011; Barlow et al. 2011a; Otani et al. 2018; Kepler et al. 2021) and other evolved stars (Kilkenny et al. 2005).

If the pulsation timing variations, τ, show periodicities, they are most likely caused by the beating of two closely spaced pulsation frequencies or reflex motion due to an unseen companion. The beating of two closely spaced frequencies, which may not be resolved in the power spectrum, causes not only sinusoidal variability in the pulsation timing but also sinusoidal variability in pulsation *amplitudes* with a phase difference of 90° (Kepler et al. 1983; Lutz 2011). If the pulsation timing variations are caused by reflex motion, the orbital solutions of the binary (or the planetary) system can be obtained from the variations. Searching for orbital solutions using this timing method has been discussed for a century since Woltger (1922) first determined the elliptic orbit of a binary star. Irwin (1952, 1959) showed that an apparent variation of an eclipsing binary period could be caused by a changing light travel time due to the reflex motion of its center of mass caused by the orbital motion of a generally more distant third star in the system. Recently, Kurtz et al. (2015) obtained the orbital solution of the unseen companion to an eclipsing binary star KIC 8569819 using this technique to verify the frequency modulation (FM) method. The FM method is similar to the PM method but it uses FM to find the orbital solution of the unseen companion.

The distance z between the object of interest and the binary system's center of gravity is generally described as

$$z = \frac{a_1 \sin i(1 - e^2)\sin(f + \varpi)}{1 + e\cos f}, \tag{2}$$

where a_1 is the length of the pulsating star orbit semimajor axis, e is the orbital eccentricity, f is the true anomaly, and ϖ is the argument of periapsis (e.g., Smart & Green (1977)). The pulsation timing variations ($\tau = z/c$) are largest when absolute values of z are also maxima, where c is the speed of light.

The true anomaly changes over time. When $e \ll 1$ (close to a circular orbit), f changes linearly over time, and is described by $f = 2\pi\nu_{\rm orb}(t - t_0)$, where $\nu_{\rm orb}$ is the orbital frequency of the sdB star, t is the time, and t_0 is the time when the pulsating star passed the argument of periapsis. Therefore, the pulsation timing variation as a function of time can be shown to be

$$\begin{aligned}\tau(t) &= \frac{a_1 \sin i}{c}\frac{(1 - e^2)\sin(2\pi\nu_{\rm orb}(t - t_0) + \varpi)}{(1 + e\cos 2\pi\nu_{\rm orb}(t - t_0))} \\ &\approx \frac{a_1 \sin i}{c}\sin(2\pi\nu_{\rm orb}(t - t_0) + \varpi).\end{aligned} \tag{3}$$

When the eccentricity e is not small enough to assume that the orbit is almost circular, the true anomaly f is not constantly changing over time. However, the trigonometric functions of true anomaly f can be described using Bessel functions (Shibahashi & Kurtz 2012) as follows:

$$\cos f = -e + \frac{2(1 - e^2)}{e}\sum_{n=1}^{\infty} J_n(ne)\cos(n2\pi\nu_{\rm orb}t), \tag{4}$$

$$\sin f = 2\sqrt{1 - e^2}\sum_{n=1}^{\infty} J_n'(ne)\sin(n2\pi\nu_{\rm orb}t), \tag{5}$$

where $J_n(x)$ is the Bessel function of the first kind of integer order n, and $J_n'(x) = \frac{dJ_n(x)}{dx}$.

Using these equations, the pulsation timing variation is described as a function of time (see Murphy et al. (2014) for the derivation) as

$$\begin{aligned}\tau(t) = \frac{1}{c}a_1 \sin i[&\textstyle\sum_{n=1}^{\infty}\xi_n(e, \varpi)\sin \\ &\times (2\pi n\nu_{\rm orb}(t - t_0) + \vartheta_n) + \tau_0(e, \varpi)],\end{aligned} \tag{6}$$

where

$$a_n(e) = \frac{2\sqrt{1 - e^2}}{e}\frac{1}{n}J_n(ne), \tag{7}$$

$$b_n(e) = \frac{2}{n}J_n'(ne), \tag{8}$$

$$\xi_n(e, \varpi) = \sqrt{(a_n(e))^2\cos^2\varpi + (b_n(e))^2\sin^2\varpi}, \tag{9}$$

$$\begin{aligned}\vartheta_n(e, \varpi) &= \tan^{-1}\left(\frac{b_n(e)}{a_n(e)}\tan\varpi\right) \\ &= \tan^{-1}\left(\frac{e}{\sqrt{1 - e^2}}\frac{J_n'(ne)}{J_n(ne)}\tan\varpi\right),\end{aligned} \tag{10}$$

and $\tau_0(e, \varpi)$ is the timing delay at $t = 0$:

$$\tau_0(e, \varpi) = -\sum_{n=1}^{\infty}\xi_n(e, \varpi)\sin\vartheta_n(e, \varpi). \tag{11}$$

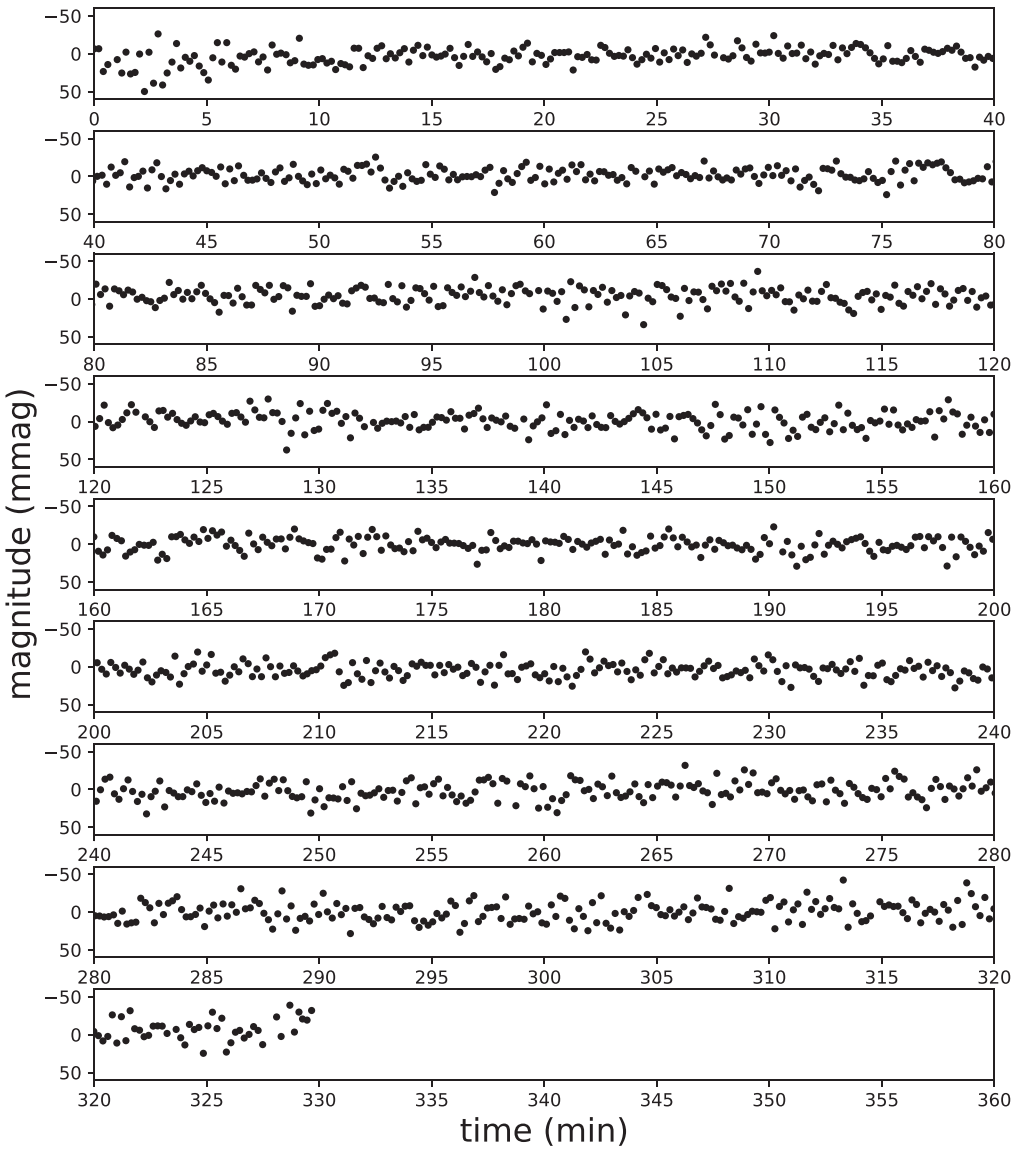

Figure 1. Example light curve for AQ Col (on 1998 February 1). The light-curve data of all observation are available as the data behind the Figure. (The data used to create this figure are available.)

For the pulsation timing variation of a sdB binary system, both the stellar evolution term, Equation (1), and the orbital motion term, Equation (6), should be considered. Also, the number of cycles, E, in Equation (1) can be described using time and pulsation period ($E = t/P$). Therefore, the complete expression for τ, is

$$\tau(t) = \frac{1}{c} a_1 \sin i \left[\sum_{n=1}^{\infty} \xi_n(e, \varpi) \sin \times (2\pi n \nu_{\rm orb}(t - t_0) + \vartheta_n) + \tau_0(e, \varpi) \right] + \frac{1}{2}\frac{\dot{P}}{P} t^2 + \frac{\Delta P}{P} t + \Delta E_o. \quad (12)$$

In Equations (11) and (12), the summation, $\sum$, will converge absolutely and the values do not significantly change after $n = 6$ for our data.

The Fourier transform of the pulsation timing variation, τ, indicates the orbital frequency $\nu_{\rm orb}$ (frequency at the Fourier transform peak) and amplitude $\frac{1}{c} a_1 \sin i$ (amplitude of the Fourier transform peak). Shibahashi & Kurtz (2012) and Murphy et al. (2014) suggest that the eccentricity, e, can be obtained from the Fourier transform of the *light curve* of the entire observation runs. In the case of $e \ll 1$, e is determined from the equations

$$e \approx \frac{2A_2}{A_1}, \quad (13)$$

or

$$e \approx \frac{4A_3}{3A_2}, \quad (14)$$

where A_1, A_2, and A_3 are the amplitudes of the first, second, and third harmonics. Therefore, A_1 is equal to the amplitude of the Fourier transform peak of the light curve. This method to obtain e is suitable particularly for the Kepler targets, that were continuously observed for more than 3 yr. However, for ground-based observations, when the targets are less frequently

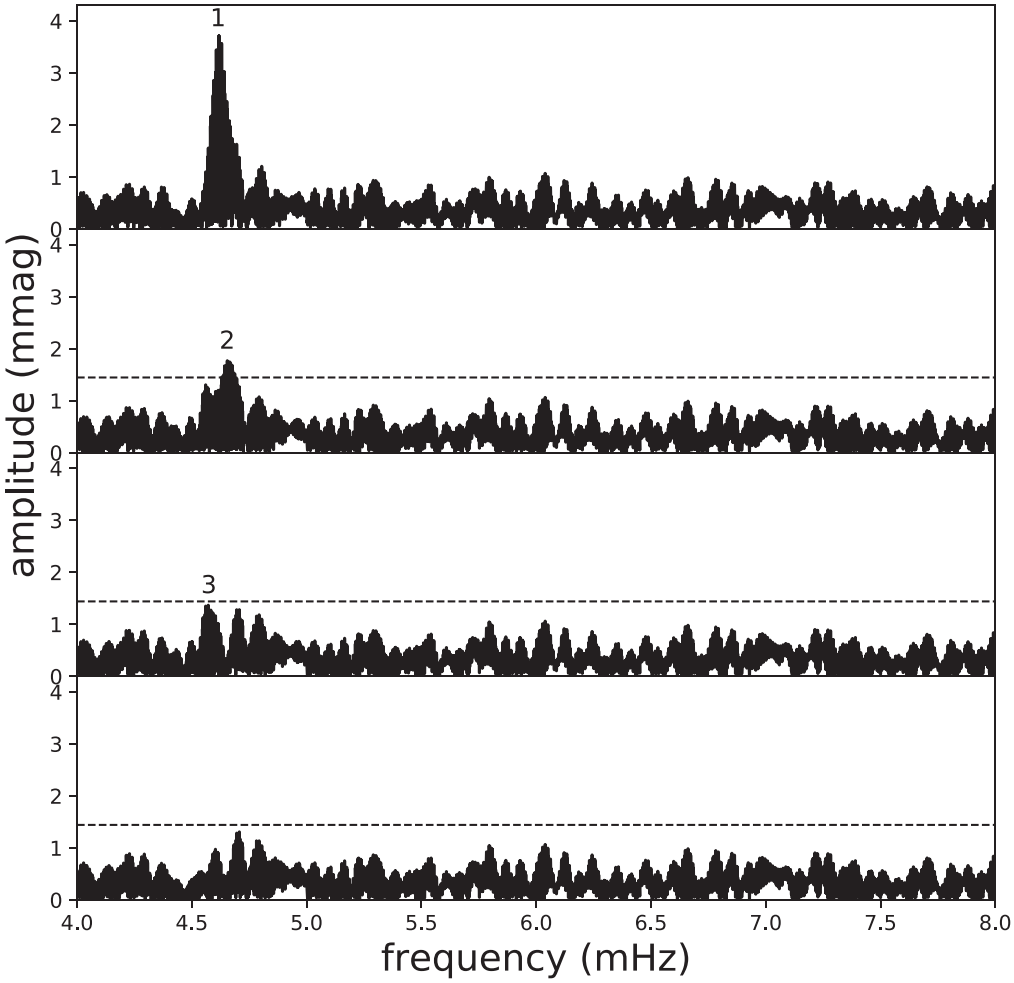

Figure 2. Example Fourier analysis for AQ Col from one of the best observing runs (combination of 1998 January 27, 28, and February 1), which indicates the difficulty in extracting the small amplitude pulsations. Three spectral peaks due to pulsation are indicated by numbers. The top panel shows the original Fourier analysis. The lower panels show the successive steps of pre-whitening by sequentially removing the next largest pulsation peaks. In each panel, the horizontal broken lines indicate 4σ noise levels; pulsations 1 and 2 are clearly above these levels, while pulsation 3 is below. Noise levels were calculated from the median Fourier amplitude after removing pulsations. Fourier transforms of data from each observing night are shown in the Figure set (five images), which is available in the online journal.

(The complete figure set (five images) is available.)

observed, the noise level of the Fourier transform of the pulsation timing variations can easily be larger than the amplitude of the harmonics. This was the case for our AQ Col data, so that e could not be constrained using Equations (13) and (14). Therefore, to constrain the value of e, ϖ, $C = \frac{\dot{P}}{P}$, $B = \frac{\Delta P}{P}$, and $A = \Delta E_o$, and t_0 in Equation (12) the pulsation timing variation data were fitted with Equation (1) and (3) using the least-squares method. Then the same pulsating timing variation data were fitted again with Equation (6) using the values of $\nu_{\rm orb}$, e, ϖ, C, B, A, and t_0 that are obtained from the previous fit as initial values.

The value $a_1 \sin i$ obtained from Equation (6) is used to calculate the mass function (Tauris & van den Heuvel 2006):

$$f = \frac{(M_2 \sin i)^3}{(M_1 + M_2)^2} = \frac{1}{2\pi G} K_1^3 P_{\rm orb} (1 - e^2)^{3/2} = \frac{(2\pi)^2}{P_{\rm orb}^2 G} (a_1 \sin i)^3 , \quad (15)$$

Table 3
Pulsation Peak Frequencies of AQ Col

Pulsation Mode	Freq (mHz)	Freq σ (mHz)	Period (s)
F1	4.6718377	1e-7	214.1
F2	4.6290798	1e-7	216.0
F3	4.5974392	4e-7	217.5

where M_1 and M_2 are the masses of the pulsating star and the unseen companion, $P_{\rm orb}$ is the orbital period, G is the gravitational constant, and $K_1 = 2\pi a_1 \sin i / P_{\rm orb} \sqrt{1 - e^2}$ is the RV amplitude of the pulsating star. This RV amplitude can be obtained from the time derivative of the position of the star, $v_{\rm rad,1} = -dz/dt$, in which z is written in Equation (2). The derivation of the RV amplitude is clearly described by Shibahashi & Kurtz (2012), Shibahashi et al. (2015), and Murphy & Shibahashi (2015). The RV and pulsation timing method are well discussed and used in Telting et al. (2012), Telting et al. (2014), Kurtz et al. (2015), Murphy et al. (2016),

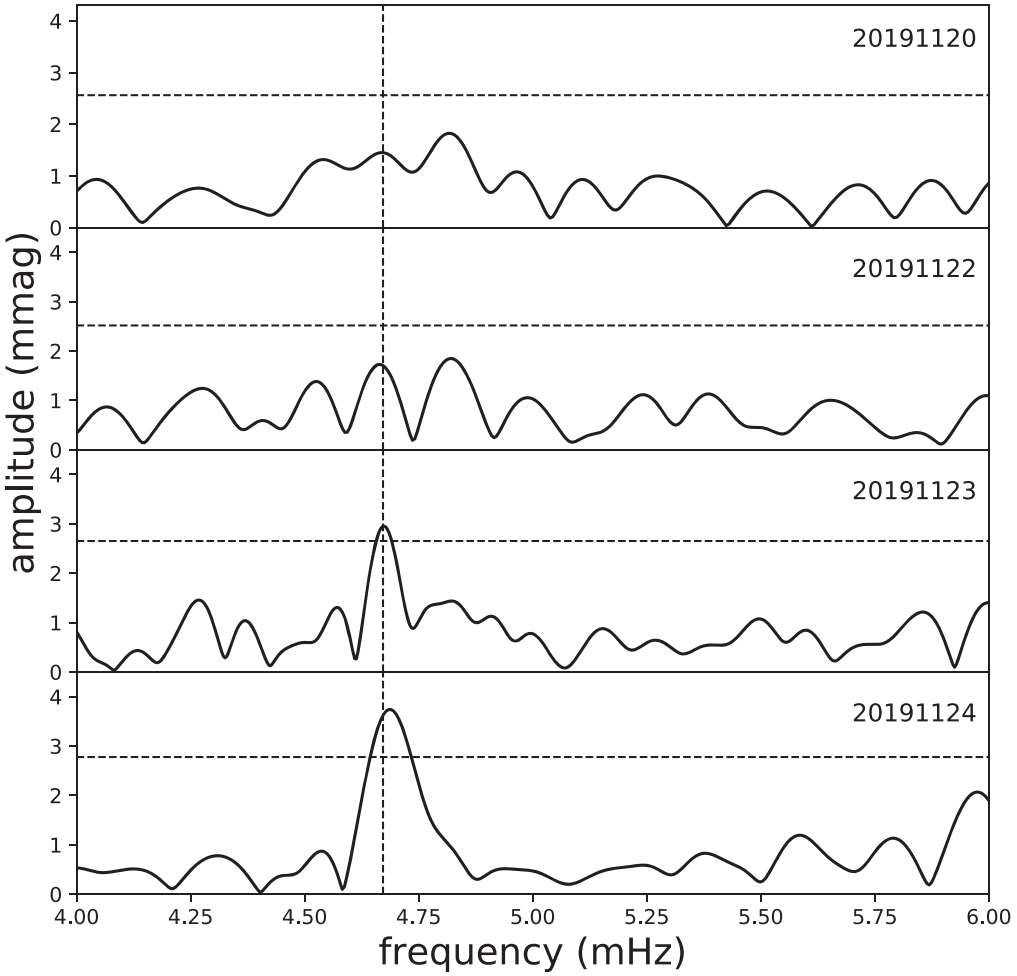

Figure 3. Fourier analysis of 4 days of observation (2019 November 20–24). The horizontal dashed lines indicate 4σ noise levels. The vertical dashed line indicates F1 (4.67 mHz). The daily amplitude variations of F1 are clearly visible. The F1 pulsation amplitude is below the 4σ noise level on November 20 and 22. Noise levels were calculated for each night; therefore, the noise level changes subtly in each panel; note that these vary slightly, reflecting weather changes from night to night and consequent quality variations in resulting light curves.

Nemec et al. (2017), Lampens et al. (2018), Murphy et al. (2018), Derekas et al. (2019), and Murphy et al. (2021).

4. Results and Discussion

4.1. Pulsation Frequencies Used

An example light curve for the night of 1998 February 1, and an amplitude spectrum for the combined data from 1998 January 27, 28, and February 1 are displayed in Figures 1 and 2. Although no pulsation is obvious in the example shown in Figure 1, the amplitude spectra of the individual data sets consistently recover the same few frequencies but with clearly variable amplitudes, as described below. The previously observed pulsation frequency range is 4.3–7.7 mHz (Koen et al. 1999; Billères & Fontaine 2005), and no new pulsation modes were found in our data. Therefore, the range between 4.0 and 8.0 mHz was plotted in Figure 2. Three pulsation peaks, which are the same within the uncertainties as the previously published frequencies, were detected above the 4σ noise levels and are listed in Table 3. Only the data in which these pulsations were detected above 4σ noise levels were used for the pulsation timing analysis. For those pulsation peaks, day-to-day pulsation amplitude changes are observed (Figure 3). Day-to-day amplitude changes were observed for other sdBV stars, such as V541 Hya, KIC 010139564, and EC 20117-4014 (Randall et al. 2009; Baran et al. 2012; Lynas-Gray 2013). Those variations can be explained by rotational splitting, and the daily amplitude variation for AQ Col also may be due to unresolved rotational splittings. The pulsation amplitude also changes from year to year (Figure 4). The recent ground-based data (2020 November–2021 January) did not show any pulsations above the noise level ($\sim$0.3 mmag) and thus they were not usable. Transiting Exoplanet Survey Satellite (TESS) space telescope also observed this target in the 20 s cadence in sectors 32 (2020 November 19–December 17) and 33 (2020 December 17–2021 January 13), a total of about 2 months. However, as shown in Figure 5, the pulsations (F1, F2, and F3) were not detected above the noise level. (Note: the pulsation amplitude is expected to be quite small in the red TESS passband. In addition to that, according to the research of a previously known pulsating DAV star HE 0532-5605, TESS cannot detect pulsations of faint, blue, compact objects if the pulsation amplitude is as small as 0.2–0.3 mmag due to the size of the telescope; Bognár et al. 2020).

4.2. Pulsation Timing Variation

Three pulsations (F1, F2, and F3) were used for the pulsation timing analysis. Data for each night were used as one data point in most cases. However, for 1998 January 27–February 1 and 2018 March 17–19, two or more nights of photometry were

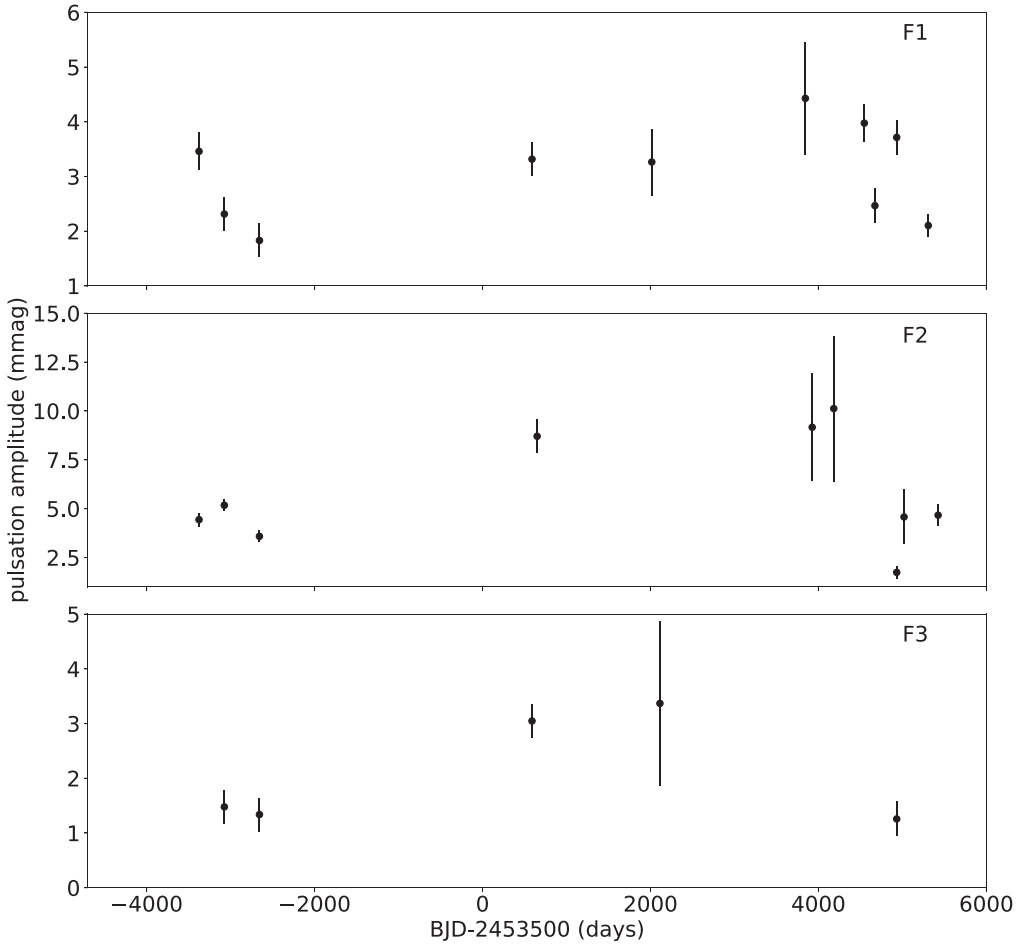

Figure 4. AQ Col seasonal pulsation amplitude variations of each pulsation mode. This diagram shows that the pulsation amplitude varies each season. TESS space telescope observed this target in 20 s cadence in sector 32 and 33 (BJD 2453500 = 5672–5727). However, pulsation was not detected above the noise level (∼0.3 mmag).

merged to obtain a better S/N. As discussed in Section 3, the secular variations—fitted here with a quadratic—show that the pulsation period is changing linearly due to the sdB's stellar evolution. We find $\dot{P}/P = 1.96 \pm 0.04 \times 10^{-7}$ yr^{-1}. The rate of period change ($\dot{P}$) indicates the age of the sdB star after the zero-age extreme horizontal branch (ZAEHB; Charpinet et al. 2002). For p-modes, $\dot{P}$ is positive during the first hot-subdwarf evolutionary phase, which is before helium in the core is exhausted. $\dot{P}$ is negative during the second evolutionary phase, which is after the depletion of helium in its core and before the post-EHB evolution. The change of sign occurs around 87–91 Myr after the ZAEHB according to Charpinet et al. (2002) models with sdB star mass ∼0.47 $M_{\odot}$. However, it also depends on the hot subdwarf formation circumstances and channel. The positive values of $\dot{P}$ for AQ Col (sdB) thus shows that the star is still in its first evolutionary phase. The age of AQ Col (sdB) can also be estimated from its effective temperature, surface gravity, mass, and mass of the H envelope. Figure 1 of Fontaine et al. (2012) also indicates that AQ Col is still in its first evolutionary phase.

The relative rate of change of the radius, can also be obtained from the timescale for the period change:

$$\frac{\dot{P}}{P} \approx \frac{3}{2}\frac{\dot{R}}{R}. \tag{16}$$

Here, R is the radius of the star. For AQ Col, the timescale for period change ($\dot{P}/P$) calculated from F1 is $(1.96 \pm 0.04) \times 10^{-7}$ yr^{-1}. This value corresponds to the relative rate of change of the radius $\dot{R}/R \approx 1.30 \times 10^{-7}$ yr^{-1}.

Figure 6 shows the time-series pulsating timing variation for F1 before and after the removal of the quadratic terms, and Figure 7 presents the phase-folded pulsation timing variation for F1, F2, and F3 after the removal of the quadratic terms. As indicated in Section 4.1, only the data in which the pulsation amplitude was larger than 4σ were used for the analysis. However, most of the data in which the pulsation amplitude is between 2σ and 4σ still match well with the solid curves in the figure, so we included those into Figures 6–8 using different colors. Table 4 lists all pulsation timing shifts for the F1, F2, and F3 pulsation modes. The solid curves in Figure 7 are the best fitting orbital solution (using only the F1 data in which the pulsation amplitude is larger than 4σ) with the actual timing shifts for F1, F2, and F3 superimposed. From Table 5, the orbital period implied by fitting the curve in Figure 7 is 486.0 ± 0.1 days, the corresponding semimajor axis (in light-seconds) and orbital eccentricity being $a_{\rm sdB} \sin i = 307.8 \pm 4.3$ and $e = 0.42 \pm 0.03$ respectively. The orbital solutions are shown in Table 5. The formal χ^2 values (only using the data in which the pulsation amplitudes are larger than 4σ) are 12.8 (F1) and 5.3 (F2). The degrees of freedom of F1 and F2 are 13 and 6. We did not calculate χ^2 for F3 because only two data points have

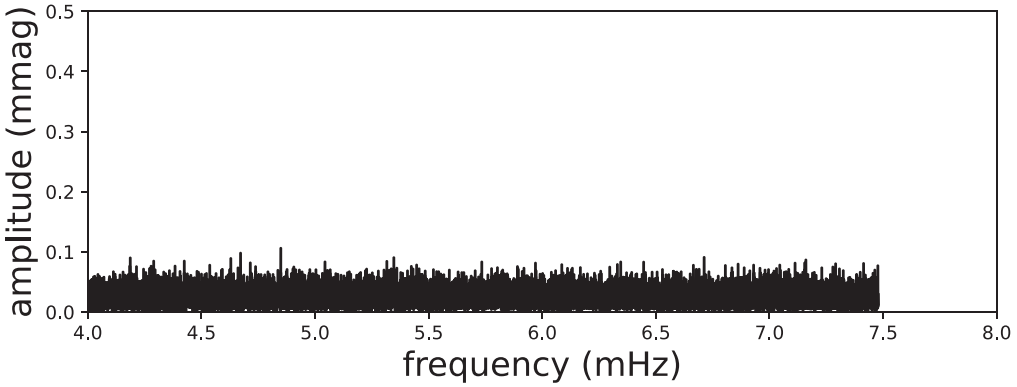

Figure 5. Fourier analysis for AQ Col from TESS sectors 32 (2020 November 19–December 17) and 33 (2020 December 17–2021 January 13) observation run. No peaks due to pulsation are indicated above the noise level (0.03 mmag).

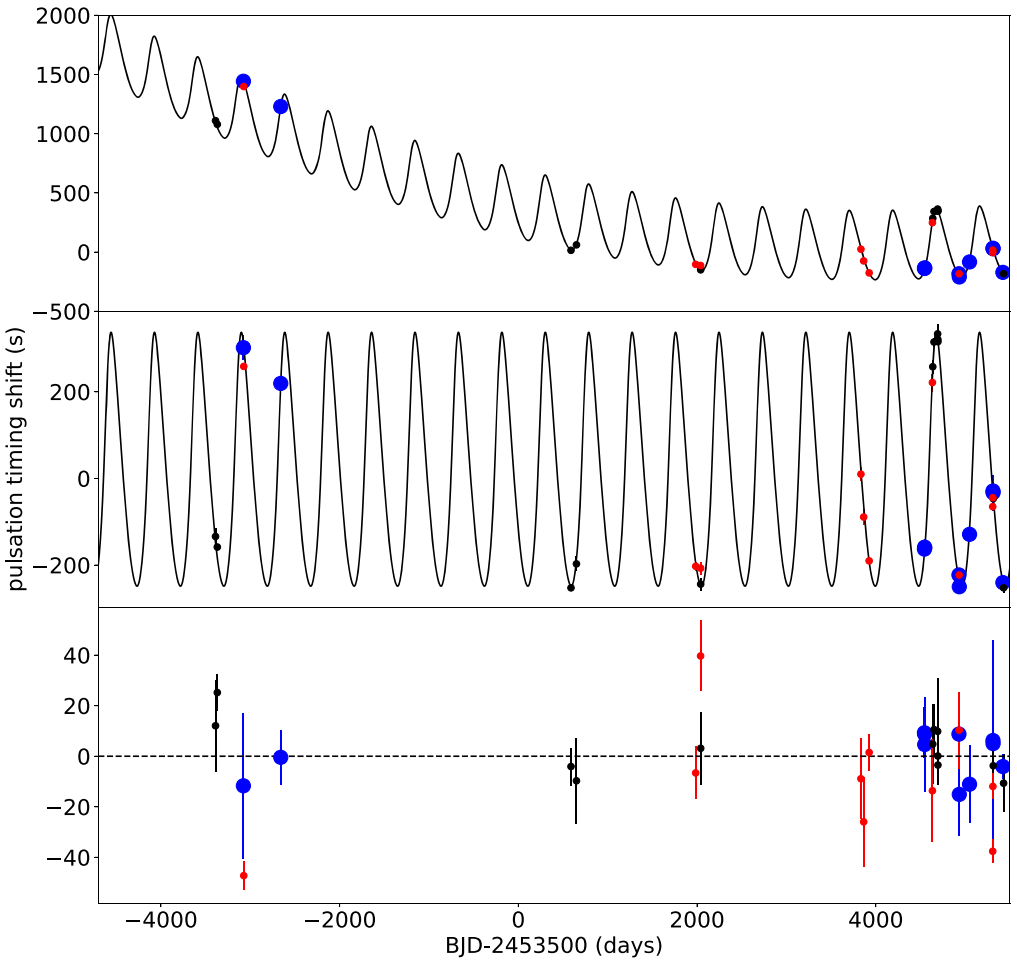

Figure 6. Top: pulsation timing variations for AQ Col constructed from the F1 pulsation at 4.67 mHz. Each dot represents the pulsating timing shift of an observation run. The timescale for period change ($\dot{P}/P$) calculated from the best-fit quadratic term is $(1.96 \pm 0.04) \times 10^{-7}$ yr^{-1}. Middle: the top diagram after the removal of the quadratic fit using Equation (6). The periods and amplitudes of the fitted curve are 486.0 days and 307.8 s. Bottom: the fit curve residuals of the middle panel. The blue dots are the data points obtained from light curves with the pulsation amplitude larger than 4σ that were used for the fittings. The black dots are the data points obtained from light curves with the pulsation amplitude between 3σ and 4σ. The red dots are the data points obtained from light curves with the pulsation amplitude between 2σ and 3σ. Pulsation timing shift uncertainties of some data points in the top and middle panels are smaller than the symbol size. Most of the data points represent 1 day of data. However, data of 1998 January 27—February 1 (BJD 2453500 = −2658.7) and 2018 March 17–19 (BJD 2453500 = 4695.2) were merged to obtain a better S/N.

pulsation amplitudes above 4σ. The corresponding right tail p values are 0.54 and 0.49. Therefore, model fits are acceptable. The χ^2 values being consistent with the number of degrees of freedom suggest that all relevant physical information has been extracted from the data.

The mass function (Equation (15)), as computed from the pulsation timing variation, is $f = 0.133 \pm 0.006\ M_\odot$. Assuming this system consists of only the sdB and long orbital period binary (please see the following sections for the triple stars possibility), for a canonical sdB star mass of $M_1 = 0.5\ M_\odot$,

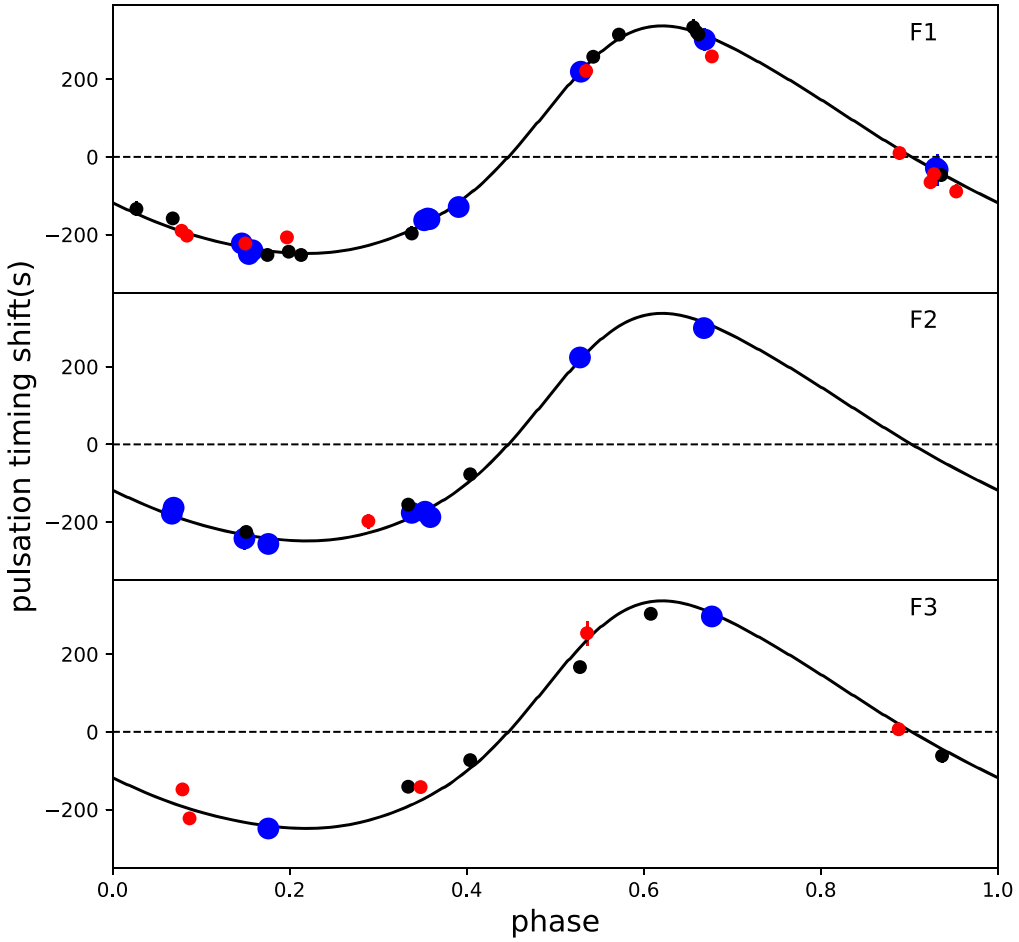

Figure 7. Phase diagram of the pulsation timing variations for AQ Col constructed from the F1, F2, and F3 pulsations (F1: 4.67 mHz at the top and F2: 4.63 mHz at the middle, F3: 4.60 mHz at the bottom). Symbols have the same meaning as in Figure 6. The orbital period implied by fitting the curve in Figure 8 is 486.0 ± 0.1 days, the corresponding semimajor axis (in light-seconds) and orbital eccentricity being $a_{\rm sdB} \sin i = 307.8 \pm 4.3$ and $e = 0.42 \pm 0.03$, respectively. Those results are listed in Table 5

substituting f and M_1 into Equation (15) gave $M_2 = 0.515 \pm 0.012\,M_\odot$ and $M_2 = 0.645 \pm 0.016\,M_\odot$ for $i = 90°$ and $i = 60°$ respectively. The estimated amplitude of the RV variations is $K_{\rm sdB} = 15.2 \pm 0.3$ km s^{-1}. Although radial velocities are difficult to measure for sdB stars because of their high gravity (which broadens the line profiles), Silvotti et al. (2020) succeeded in measuring the RVs of sdB stars to a precision of $\approx$100 m s^{-1} (5σ level) using High Accuracy Radial velocity Planet Searcher for the Northern hemisphere (HARPS-N) at the 3.6 m Telescopio Nazionale Galileo. The RV amplitude of AQ Col due to the existence of the long orbital period binary is much larger than this, and it should be possible to confirm the companion using the RV method.

When the period of the pulsation timing variation matches with the pulsation *amplitude* variation, the pulsation timing variation may be due to two closely spaced pulsation frequencies (Lutz 2011). However, this is not the case. The period of the pulsation timing variation ($P = 486.0$ days) does not match with the F1, F2 pulsation amplitude variations and the pulsation amplitude variations' shapes are not sinusoidal, so this is not due to the beating of two closely spaced pulsation frequencies (see Figure 4). Therefore, we conclude that the resulting pulsation timing variations in Figures 6 and 7 are due to the light-travel effects caused by an unseen companion.

4.3. Spectroscopy

As noted in Table 2, AQ Col was found to have a large and rapid RV variation. In particular, spectra obtained on 1996 December 5 showed an RV change of $\sim$50 km s^{-1} in 45 minutes. An orbital period of 486 days, identified through photometry, corresponds to a sdB star RV amplitude of 15.2 ± 0.3 km s^{-1} (Table 5), smaller than the RV change observed on 1996 December 5. We have therefore considered AQ Col to be a triple star, the long period binary identified photometrically having a sdB component which is a short period binary, and proceeded to analyze our reduced spectra on this basis.

During four 1200 s exposures, resulting in the two spectra obtained on 1996 December 5th, orbital motion would in this case have resulted in significant Balmer line broadening. We therefore decided to confine our spectroscopic analysis to the two spectra obtained in 1996 December; these were shifted into an observer's rest frame and added with equal weight. Balmer line broadening by orbital motion was found to be well represented by convolution with a Gaussian having an FWHM = 0.5 Å. In determining the equivalent FWHM, a time-dependent linear change in RV (sampled at 0.1 s intervals) was assumed during the sequence of arc and science exposures.

Near-photometric conditions prevailed at the SAAO Sutherland site on 1996 December 5, and a small wavelength-dependent correction was applied using available photometry.

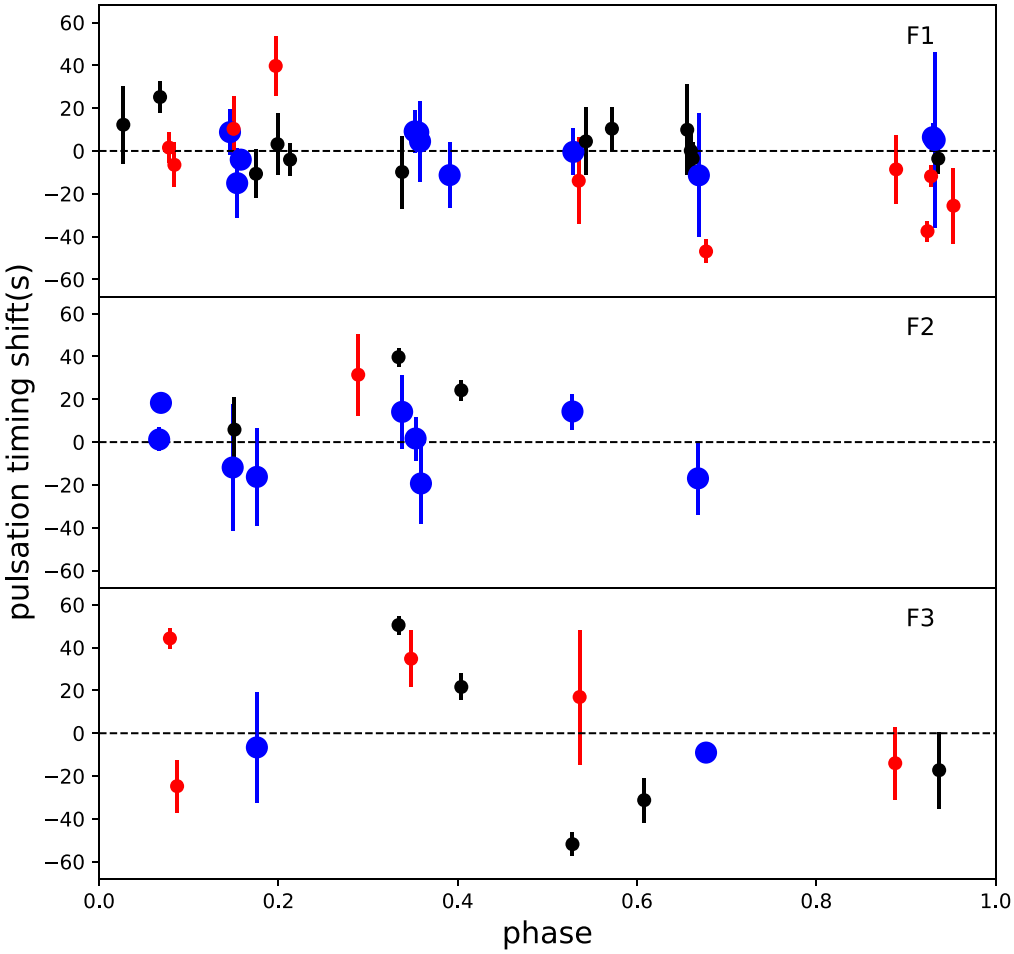

Figure 8. Residuals of the pulsating timing variations after subtracting the fit shown in Figure 7. The top panel shows the residuals of F1, the middle panel shows the residuals of F2, and the bottom panel shows the residual of F3. Symbols have the same meaning as in Figure 6

UBV fluxes were obtained from the EC Survey (O'Donoghue et al. 2013) and zero-points of 20.94, 20.51, and 21.12 for *U*, *B*, and *V,* respectively, with these being derived from the Hayes & Latham (1975) flux calibration and the Kurucz (1979) model atmosphere for Vega. While the *UBV* flux calibration is dated, it proved to be consistent with the Gaia *G*-Band flux density (Riello et al. 2021) and adequate for our purposes, given other uncertainties involved.

Bailer-Jones et al. (2021) obtain 1.54 $^{+0.10}_{-0.07}$ kpc as the AQ Col distance, with its galactic coordinates ($\ell = 243.^{\circ}84$, $b = -33.^{\circ}84$), the Arenou et al. (1992) galactic extinction map gives $E_{B-V} = 0.06 \pm 0.05$, assuming $R = 3.1$. Adopting $E_{B-V} = 0.06$, both the spectral energy distribution and flux density points have been dereddened using Seaton's (1979) calibration and Howarth's (1983) extension of it into the optical and infrared regions. Figure 9 shows the dereddened AQ Col energy distribution obtained from 1996 December spectra plotted as a black line. Green squares show the dereddened Johnson *B*- and Gaia *G*-band flux densities for comparison.

Spectra obtained on 1989 December 21 and 1996 December 5 were *quick look* spectra obtained with a Reticon detector and taken for classification purposes as part of the EC survey (Stobie et al. 1997). No special attention was accordingly given to the removal of *fixed pattern* noise known to be present in Reticon spectra as, for example, Timothy (1983) discusses. A comparison between the combined spectrum plotted in Figure 10 and the AQ Col spectrum Koen et al. (1999, their Figure 7) publish, demonstrates a probable non-astrophysical origin for the apparent structure in the Figure 10 spectrum. We accordingly analyze the Figure 10 spectrum on the basis that only Balmer lines are present, as indicated by CCD spectra, one obtained by ourselves with the SOAR 4.1 m telescope and the other which Koen et al. publish.

The red line in Figure 9 is the non-LTE model atmosphere emergent energy distribution from the Németh et al. (2014) grid for $T_{\rm eff} = 30{,}000$ K, $\log g = 5.9$ and $\log(N({\rm He})/N({\rm H})) = -5.0$, successively broadened by two Gaussians having FWHM = 0.5 Å and FWHM = 3.5 Å to allow for orbital and instrumental broadening respectively. Trial rotation-broadening profiles were calculated for selected $v \sin i$ values following, for example, Underhill (1968) and adopting a gray atmosphere limb darkening; the result was convolved with the synthetic spectrum for the fitted effective temperature and surface gravity for subsequent comparison with observation. At our low resolution, Balmer line cores are not very sensitive to stellar rotation and we therefore have a large error in the determination of $v \sin i = 300 \pm 100$ (km s^{-1}). The Figure 9 model spectrum has therefore also been broadened by a rotation profile corresponding to $v \sin i = 300$ km s^{-1}. Our model spectrum plotted in Figure 9 is the best agreement with observation we achieved; other comparisons gave standard error limits of $\delta(T_{\rm eff}) = \pm 2000$K and $\delta(\log g) = \pm 0.2$. The absence of He I lines and the good fit

Table 4
Pulsation Timing Variation Data for F1 (4.67 mHz), F2 (4.63 mHz), and F3 (4.60 mHz) Pulsation Modes After Removing the Quadratic Fits

Time (BJD 2453500)	F1 (s)	σ (F1) (s)	F2 (s)	σ (F2) (s)	F3 (s)	σ (F3) (s)
-3388.61	−133.9	18.2	…	…	…	…
-3368.71	−158.3	7.3	−178.4	5.4	…	…
-3367.63	…	…	−163.0	4.2	…	…
-3076.56	301.9	28.7	299.3	17.2	…	…
-3072.57	258.6	5.6	…	…	297.0	4.1
-2658.69	219.3	10.7	223.7	8.2	166.7	5.6
589.39	−252.5	7.5	…	…	…	…
650.33	−197.1	16.9	−176.2	17.1	…	…
1984.79	−202.7	10.4	…	…	…	…
1985.69	…	…	…	…	−222.6	12.3
2039.70	−207.2	13.9	…	…	…	…
2040.69	−244.0	14.3	…	…	…	…
2112.61	…	…	…	…	−142.1	13.3
3832.65	…	…	…	…	6.7	16.9
3833.74	9.9	15.9	…	…	…	…
3864.70	−89.0	17.7	…	…	…	…
3925.70	−190.2	7.2	…	…	−148.1	4.8
4182.77	…	…	…	…	303.8	10.4
4544.56	−163.1	10.0	−173.3	10.1	…	…
4546.52	−158.6	1.7	…	…	…	…
4547.55	−160.2	18.7	−187.1	18.9	…	…
4633.72	221.4	20.2	…	…	254.0	31.5
4637.64	257.8	15.8	…	…	…	
4651.61	314.9	10.0	…	…	…	…
4692.29	333.7	21.1	…	…	…	…
4694.28	320.9	10.4	…	…	…	…
4695.24	315.7	7.3	…	…	…	…
4930.55	−222.8	10.7	…	…	…	…
4931.51	…	…	−242.2	29.7	…	…
4932.55	−222.9	15.1	−225.4	15.3	…	…
4934.53	−249.9	16.3	…	…	…	…
4999.70	…	…	−197.6	19.1	…	…
5021.34	…	…	−155.1	4.4	−141.2	4.4
5049.31	−129.0	15.3	…	…	…	…
5055.30	…	…	−77.0	4.8	−72.8	6.1
5308.51	−65.1	4.7	…	…	…	…
5310.46	−44.5	5.0	…	…	…	…
5311.50	−29.0	6.3	…	…	…	…
5312.48	−32.8	41.1	…	…	…	…
5314.51	−46.7	7.1	…	…	−61.6	18.0
5422.30	−240.4	4.8	…	…	…	…
5430.28	−252.4	11.3	−256.3	…	…	…

Note. All data points obtained from light curves with the pulsation amplitudes larger than 2σ are listed. Time is mid-observing time.

(This table is available in its entirety in machine-readable form.)

obtained with $\log(N(\mathrm{He})/N(\mathrm{H})) = -5.0$ indicates that this may be a helium abundance upper limit.

Synthetic spectrum fitting involved normalization to the Johnson *V*-band flux at 5540 Å, corresponding to a hot subdwarf angular radius of $\alpha = (2.6 \pm 0.1) \times 10^{-12}$ radians. The uncertainty in α follows from the $T_{\rm eff}$ and reddening correction errors. Given the Bailer-Jones et al. distance, the hot subdwarf radius, mass, and luminosity were then found to be $0.18 \pm 0.01\,R_\odot$, $0.91 \pm 0.44\,M_\odot$, and $24 \pm 7\,L_\odot$ respectively. Associating the measured angular radius with a stellar radius implies that AQ Col is a spherical star; with $v \sin i = 300$ km s^{-1} this may not be the case and could have led to an erroneous high mass.

Table 5
Orbital Information of the AQ Col System

Parameters	Values
Period, P (days)	486.0 ± 0.1
Amplitude, $a_{\rm sdB} \sin i$ (*s*)	307.8 ± 4.3
Eccentricity, e	0.42 ± 0.03
Argument of periapsis, ϖ (rad)	0.72 ± 0.05
Zero point of time, t_0 (BJD 2453500)	262.5 ± 3.6
Mass function, $f\,(M_\odot)$	0.133 ± 0.006
RV for sdB star, $K_{\rm sdB}$ (km s^{-1})	15.2 ± 0.3

4.4. Unseen Companions

Most sdB stars in binary systems have companions which are white dwarfs or M-dwarf main-sequence stars (Kupfer et al. 2015); these have short orbital periods ($\lesssim$10 days) and are believed to be post-common envelope systems (Han et al. 2002, 2003; Xiong et al. 2017). Some sdB binaries have longer orbital periods with an F- or G-type giant or main-sequence star and 26 of those systems have been studied so far (Vos et al. 2018, 2019a). Following Han et al. (2002, 2003), sdB stars in long period binaries are formed as a consequence of a red giant progenitor losing almost all of its hydrogen-rich envelope, at the onset of core helium burning, through stable Roche lobe overflow (RLOF); their calculations suggest that the orbits should be circular and have periods $\lesssim$500 days. However, RV observations by Østensen & Van Winckel (2012), Deca et al. (2012), Barlow et al. (2012), and Wade et al. (2014), identified sdB stars having a main-sequence or giant companion with orbital periods >500 days, significantly greater than the Han et al. (2002, 2003) orbital-period distribution would suggest. Chen et al. (2013) reproduce the orbital-period distribution observed by Østensen & Van Winckel (2012) using detailed binary evolution calculations for the stable RLOF channel, improving on the simplified binary population synthesis by Han et al. (2003). Vos et al. (2018, 2020) also performed a binary population synthesis study, and the estimated period of binaries that went through this RLOF channel is $P = 400$–1500 days, and eccentricity $e = 0$–0.3 (see Figure 3 of Vos et al. 2019b and Figure 4 of Molina et al. 2021). The orbital period of the long orbital period companion to AQ Col ($P = 486.0$ days) falls in the middle of this range, however the eccentricity ($e = 0.424$) does not fall in the range. That suggests that this system in not a typical sdB+MS binary system. This high eccentricity might be caused by the presence of a close companion which was discussed in Section 4.3. The common envelope system might cause a large amount of mass loss from the system that the outer companion could not efficiently accrete and its orbit was not efficiently circularized. If AQ Col is eventually confirmed to be a triple star as proposed in the present paper, the two-star RLOF model needs an adaptation dependent on better component mass determinations. Triple star evolution is an active field of research lagging behind studies of binary and single star evolution as Toonen et al. (2020) discuss. An interesting result from the Toonen et al. study is the fact that about 40% of triple-star systems retain eccentric orbits, before RLOF if it occurs, which would be consistent with our determination of $e = 0.42 \pm 0.03$ for the orbit of the unseen more distant component.

Figure 10 shows the color–color diagram (*u*–*z* versus *z*–W1) of known sdB binary systems. The Skymapper *u* and *z* and Wide-field Infrared Survey Explorer (WISE) W1 magnitudes

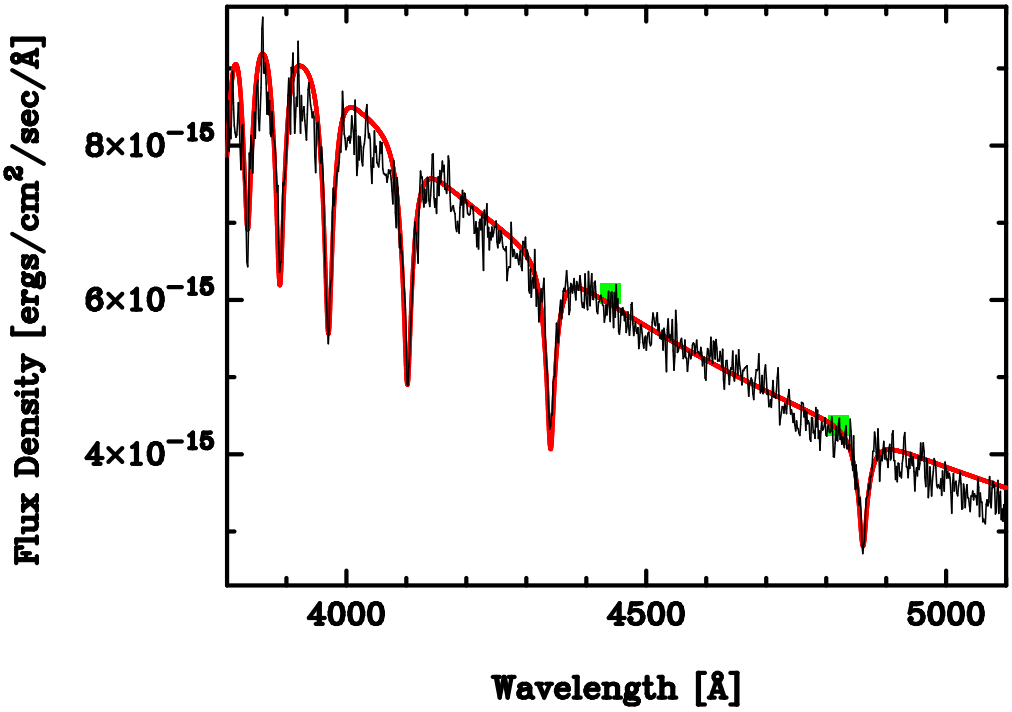

Figure 9. Two spectra obtained on 1996 December 5 combined after shifting into an observer's rest frame, compared with a non-LTE model spectrum for $T_{\rm eff} = 30{,}000$ K, $\log g = 5.9$, $\log(N({\rm He})/N({\rm H})) = -5.0$ and $v \sin i = 300$. Green squares show the dereddened Johnson B- and Gaia G-band flux densities for comparison. See the text for details.

are used (Keller et al. 2007; Wright et al. 2010). In this diagram, the colors of AQ Col are compared with single sdB stars, sdB+MS, sdB+dM, and sdB+WD. All the available data used are from the hot subdwarf database (Geier et al. 2019). This diagram suggests that the AQ Col system is not likely to be a sdB+dM or sdB+MS system and the color is bluer than other known sdB+WD systems. The known single sdBs spread even into the sdB+MS regions, and those might actually be binary systems.

This result is the same for the GAIA color. The GAIA color $G_{\rm BP} - G_{\rm RP} = -0.435$ and absolute magnitude $M_{\rm G} = 4.52$ for AQ Col, neglecting a small reddening correction, places it among the apparently single sdB and sdOB stars in the color–magnitude diagram Geier et al. (2019, their Figure 3, right-hand panel) publish and verifying their suggestion that some of these could also be binary (or multiple) systems.

As discussed in the Section 4.3, Spectra obtained on 1996 December 5 exhibit a change of 49.1 km s^{-1} in 46.1 minutes, which cannot be a consequence of the wide binary inferred through the light-travel-time analysis. Instead, we suggest the hot subdwarf in the AQ Col wide binary is itself a close binary. If the close-binary orbit were circular, coplanar with the line of sight, and the hot subdwarf had an orbital speed about this center of mass of ∼220 km s^{-1}, as Table 2 spectra from 1989 and 2020 seem to suggest, an unseen companion would have a mass of $\sim 1.4\,M_\odot$ for a canonical hot subdwarf mass of $\sim 0.5\,M_\odot$; a systemic velocity of zero has been adopted, the barycentric correction relative to the solar system barycenter is ∼0.1 km s^{-1} and has been neglected. If the hot subdwarf orbital speed were 300 km s^{-1}, which could be the case if an orbit were highly inclined, the companion mass would be $\sim 3.0\,M_\odot$. Estimated orbital periods range from 0.7–1.1 days for the 220 and 300 km s^{-1} cases, respectively. Varying the assumed systemic velocity by ±10 km s^{-1} and the canonical hot subdwarf mass by $\pm 0.1\,M_\odot$ alters the estimated companion mass by ∼0.05 and $\sim 0.1\,M_\odot$ respectively. If the AQ Col sdB star in a wide binary itself forms a close binary with a $1.4\,M_\odot$ companion, for example, then with $f = 0.133 \pm 0.006\,M_\odot$ and $M_1 = 1.9\,M_\odot$, substituting f and M_1 into Equation (15) gave wide binary companion masses of $M_2 \simeq 1.05 \pm 0.02\,M_\odot$ and $M_2 \simeq 1.27 \pm 0.02\,M_\odot$ for $i = 90°$ and $i = 60°$, respectively. If the inclination is below $i = 53.8°$, the mass of the wide binary would be larger than the Chandrasekhar limit ($M_2 = 1.40\,M_\odot$).

To date, several circumbinary planetary systems or brown dwarf systems candidates are discussed using the eclipse timing method (Pulley et al. 2018, and references therein). However those long period companions have smaller O–C amplitudes than the long orbital period companion to AQ Col, which indicates that the long orbital period companion to AQ Col should have much larger mass. For this reason, AQ Col may be an interesting triple star system candidate to continue monitoring—if pulsation persists. Wu et al. (2018, 2020) presented mass-transfer processes from a primordial binary that evolves into an sdB+NS system. This theory estimates about 7000–21000 sdB+NS binaries in the Galaxy at the present epoch, which contributes 0.3%–0.5% of the total sdB binaries, but no sdB+NS binary system is known yet.

5. Conclusions

This paper discusses the photometric and spectroscopic properties of the sdB star, AQ Col. Photometric data of AQ Col for 25 yr show obvious periodic variations in the three largest amplitude pulsation frequencies and allowed us to obtain an orbital solution for the long period companion using the pulsation timing method. We find this long orbital period system to have the following properties:

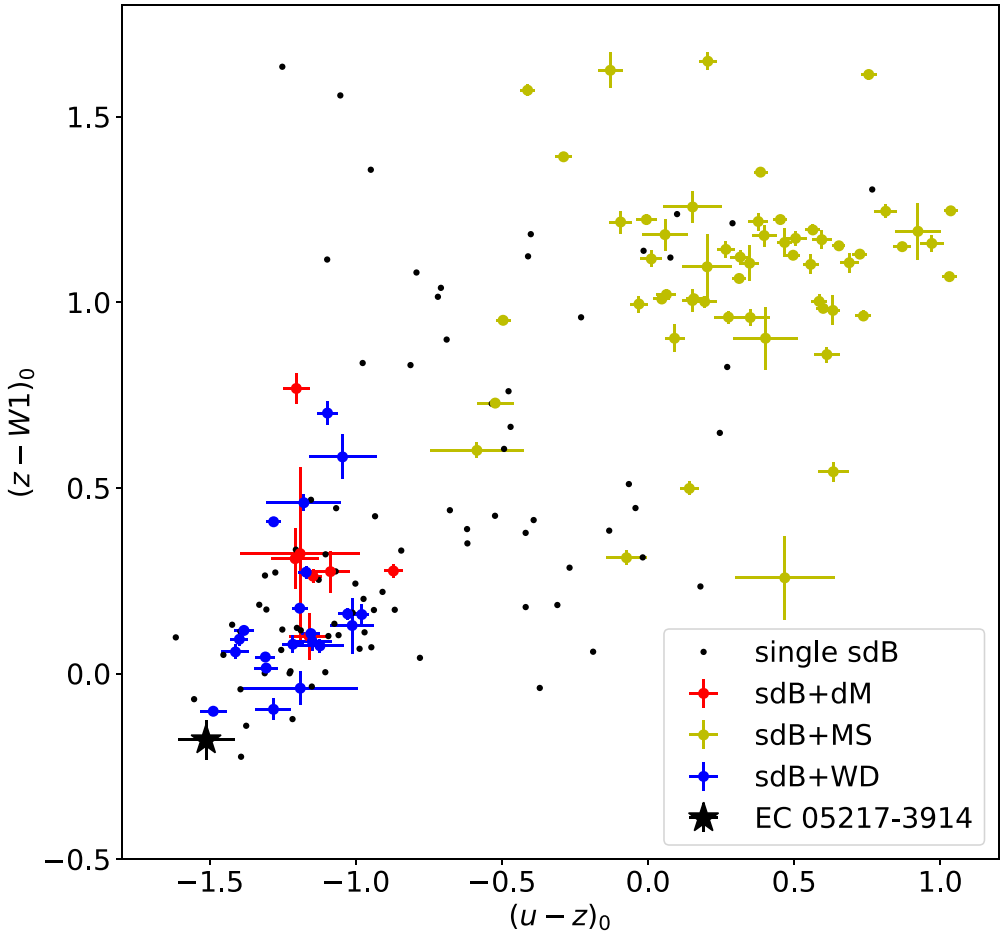

Figure 10. Skymapper/WISE *u*–z vs. *z*–W1 color–color diagram (colors dereddened). The black, red, yellow, and blue symbols show the single sdB stars, sdB+dM, sdB+MS, and sdB+WD, respectively. The AQ Col sdB binary candidate is indicated with a black star symbol. All stars except single sdB stars have uncertainties which are indicated by the cross marks. Those empirical data are taken from all available data in the subdwarf database (Geier et al. 2019).

1. Orbital period $P = 486.0 \pm 0.1$ days
2. Eccentricity $e = 0.42 \pm 0.03$, which is extremely high compared with other sdB+MS binary systems, and suggests that this system is not a typical sdB+MS binary.
3. The light-travel time amplitude $A = 307.8 \pm 4.3$ s
4. The expected RV amplitude of the sdB star due to this companion is $K_{\rm sdB} = 15.2 \pm 0.3$ km s^{-1}

However, available spectra show the minimum RV amplitude is ∼300 km s^{-1}, which cannot be reconciled with the estimated RV amplitude ($K_{\rm sdB} = 15.2 \pm 0.3$ km s^{-1}). This discrepancy suggests that AQ Col may be a triple system with both a long period ($P = 486$ days) and a possible short period ($P \leqslant 10$ days) companion, the latter of which is below the detection limits using the pulsation timing analysis. Our color–color diagram shows that one of the companions is likely to be a white dwarf or another hot and faint object. Since those systems have not been studied well yet, AQ Col is a unique system that should be monitored in the future.

Pelisoli et al. (2021) find HD 265435 to be a possible supernova Ia progenitor, and AQ Col could be similar. Further AQ Col RV observations are needed to confirm that this wide binary has a hot subdwarf which itself is a close binary whose components have a combined mass that exceeds the Chandrasekhar mass.

An anonymous referee has provided valuable insight through questions posed in a report on the first submitted draft of this paper, and for which the authors are most grateful. T.O. acknowledges research support from the National Aeronautics and Space Administration (NASA) under grant No. 80NSSC21K0245 and the National Science Foundation (NSF) under grant No. AST-2108975. T.O. is indebted to Andy Baran for suggestions by the pulsation timing technique could be improved. D.K. thanks the University of the Western Cape for financial assistance. T.v. H. acknowledges research support from the National Science Foundation under grant No. AST-1715718. M.U. acknowledges financial support from CONICYT Doctorado Nacional in the form of grant No. 21190886 and ESO studentship program. This paper uses observations made at the SARA-CT telescope at the Cerro Tololo Inter-American Observatory (CTIO). This paper uses observations made at the SAAO. This paper includes data collected by the TESS mission. Funding for the TESS mission is provided by the NASA Explorer Program. Based on observations obtained at the SOAR telescope under the program allocated by the Chilean Time Allocation Committee (CNTAC), No. CN2020A-87.

Facilities: SAAO: 0.5 m, SAAO: 0.75 m, SAAO: 1.0 m, SAAO:1.9 m, SOAR:4.1 m, CTIO:0.6 m, TESS

Software: DoPhot (Schechter et al. 1993, in an automated form), Period04 (Lenz 2004), and AstroImageJ (Collins et al. 2017)

ORCID iDs

T. Otani https://orcid.org/0000-0002-1691-8479
T. von Hippel https://orcid.org/0000-0002-5775-2866
M. Uzundag https://orcid.org/0000-0002-6603-994X
M. Vučković https://orcid.org/0000-0001-8339-6423
C. M. Pennock https://orcid.org/0000-0003-2164-5337

References

Applegate, J. H. 1992, ApJ, 385, 621
Arenou, F., Grenon, M., & Gomez, A. 1992, A&A, 258, 104
Bailer-Jones, C. A. L., Rybizki, J., Fouesneau, M., Demleitner, M., & Andrae, R. 2021, AJ, 161, 147
Baran, A. S., Reed, M. D., Stello, D., et al. 2012, MNRAS, 424, 2686
Barlow, B. N., Dunlap, B. H., Clemens, J. C., et al. 2011a, MNRAS, 414, 3434
Barlow, B. N., Dunlap, B. H., & Clemens, J. C. 2011b, ApJL, 737, L2
Barlow, B. N., Liss, S. E., Wade, R. A., & Green, E. M. 2012, ApJ, 771, 23
Bergeron, P., Wesemael, F., Beauchamp, A., et al. 1994, ApJ, 432, 305
Billères, M., & Fontaine, G. 2005, in ASP Conf. Ser. 334, 14th European Workshop on White Dwarfs, ed. D. Koester & S. Moehler (San Francisco, CA: ASP), 635
Blackman, R. B., & Tukey, J. W. 1958, Bell Syst. Tech. J., 37, 185
Bognár, Zs, Kawaler, S. D., Bell, K. J., et al. 2020, A&A, 638, A82
Bonanno, A., Catalano, S., Frasca, A., Mignemi, G., & Paternò, L. 2003, A&A, 398, 283
Bours, M. C. P., Marsh, T. R., Parsons, V. S., et al. 2016, MNRAS, 460, 3873
Charpinet, S., Fontaint, G., Brassard, P., & Dorman, B. 1996, ApJL, 471, L103
Charpinet, S., Fontaine, G., Brassard, P., & Dorman, B. 2000, ApJS, 131, 223
Charpinet, S., Fontaint, G., Brassard, P., & Dorman, B. 2002, ApJS, 140, 469
Chen, X., Han, Z., Deca, J., & Podsiadlowski, P. 2013, MNRAS, 434, 186
Clausen, D., & Wade, R. A. 2011, ApJL, 733, L42
Clemens, J. C., Crain, J. A., & Anderson, R. 2004, Proc. SPIE, 5492, 331
Collins, K. A., Kielkopf, J. F., Stassun, K. G., & Hessman, F. V. 2017, AJ, 153, 2
Costa, J. E. S., & Kepler, S. O. 2008, A&A, 489, 1225
Dalessio, J. R. 2013, PhD thesis, Univ. Delaware
D'Cruz, N. L., Dorman, B., Rood, R. T., et al. 1996, ApJ, 466, 359
Deca, J., Marsh, T. R., Østensen, R. H., & O'Connell, R. W 2012, MNRAS, 421, 2798
Derekas, A., Murphy, S. J., Dálya, G., et al. 2019, MNRAS, 486, 2129
Dorman, B., Rood, R. T., & O'Connell, R. W. 1993, ApJ, 419, 596
Eastman, J., Siverd, R., & Gaudi, S. B. 2010, PASP, 122, 935
Fontaine, G., Brassard, P., Charpinet, S., et al. 2012, A&A, 539, 12
Geier, S., Raddi, R., Gentile Fusillo, N. P., & Marsh, T. R. 2019, A&A, 621, 38
Green, E. M., Fontaine, G., Reed, M. D., et al. 2003, ApJ, 583, 31
Han, Z., Podsiadlowski, Ph., Maxted, P. F. L., & Marsh, T. R. 2003, MNRAS, 341, 669
Han, Z., Podsiadlowski, Ph., Maxted, P. F. L., Marsh, T. R., & Ivanova, N. 2002, MNRAS, 336, 449
Hayes, D. S., & Latham, D. W. 1975, ApJ, 197, 593
Heber, U. 2009, ARA&A, 47, 211
Howarth, I. D. 1983, MNRAS, 203, 301
Irwin, J. B. 1952, ApJ, 116, 211
Irwin, J. B. 1959, AJ, 64, 149
Jorden, A. R., Read, P. D., & van Breda, I. G. 1982, Proc. SPIE, 331, 368
Keel, W. C., Oswalt, T., Mack, P., et al. 2017, PASP, 129, 015002
Keller, S. C., Schmidt, B. P., Bessell, M. S., et al. 2007, PASA, 24, 1
Kepler, S. O., Robinson, E. L., & Nather, R. E. 1983, ApJ, 271, 744
Kepler, S. O., Winget, D. E., Nather, R. E., et al. 1991, ApJL, 378, L45
Kepler, S. O., Winget, D. E., Vanderbosch, Z. P., et al. 2021, ApJ, 906, 7
Kilkenny, D. 2010, Ap&SS, 329, 175
Kilkenny, D., Crause, L., & van Wyk, F. 2005, MNRAS, 361, 559
Kilkenny, D., Fontaine, G., Green, E. M., & Schuh, S. 2010, IBVS, 5927, 1
Kilkenny, D., O'Donoghue, D., Koen, C., Stobie, R. S., & Chen, A. 1997, MNRAS, 287, 867
Kilkenny, D., Worters, H. L., O'Donoghue, D., et al. 2016, MNRAS, 459, 4343
Koen, C. 1998, MNRAS, 300, 567
Koen, C., O'Donoghue, D., Kilkenny, D., Stobie, R. S., & Saffer, R. A. 1999, MNRAS, 306, 213
Kupfer, T., Geier, S., Heber, U., et al. 2015, A&A, 576, A44
Kurtz, D. W., Humbleton, K. M., Shibahashi, H., Murphy, S. J., & Prša, A. 2015, MNRAS, 446, 1223
Kurucz, R. L. 1979, ApJS, 40, 1
Lampens, P., Frémat, Y., Vermeylen, L., et al. 2018, A&A, 610, A17
Lenz, P. 2004, CoAst, 144, 41
Lutz, R. 2011, PhD thesis, Georg-August-Universität
Lynas-Gray, A. E. 2013, in ASP Conf. Ser. 479, Progress in Physics of the Sun and Stars: A New Era in Helio- and Asteroseismology, ed. H. Shibahashi & A. E. Lynas-Gray (San Francisco, CA: ASP), 273
Mackebrandt, F., Schuh, S., Silvotti, R., et al. 2020, A&A, 638, 108
Molina, F., Vos, J., Németh, P., et al. 2021, A&A, in press (arXiv:2110.14339)
Mullally, F., Winget, D. E., Degennaro, S., et al. 2008, ApJ, 676, 573
Murphy, S. J., Bedding, T. R., Shibahashi, H., Kurtz, D. W., & Kjeldsen, H. 2014, MNRAS, 441, 2515
Murphy, S. J., Maxwell, M., Kurtz, D. W., et al. 2018, MNRAS, 474, 4322
Murphy, S. J., & Shibahashi, H. 2015, MNRAS, 450, 4475
Murphy, S. J., Shibahashi, H., & Bedding, T. R. 2016, MNRAS, 461, 4215
Murphy, S. J., Tanda, L., Sanjay, S., et al. 2021, MNRAS, 505, 2336
Nemec, J. M., Balona, L. A., Murphy, S. J., Kinemuchi, K., & Young-Beom, J. 2017, MNRAS, 466, 1290
Németh, P., Østensen, R., Tremblay, P., & Hubeny, I. 2014, in ASP Conf. Ser. 481, 6th Meeting on Hot Subdwarf Stars and Related Objects, ed. V. van Grootel et al. (San Francisco, CA: ASP), 95
O'Donoghue, D., Kilkenny, D., Koen, C., et al. 2013, MNRAS, 431, 240
O'Donoghue, D., Koen, C., & Kilkenny, D. 1996, MNRAS, 278, 1075
O'Donoghue, D., Lynas-Gray, A. E., Kilkenny, D., Stobie, R. S., & Koen, C. 1997, MNRAS, 285, 657
Oreiro, R., Ulla, A., Pérez Hernández, F., et al. 2004, A&A, 418, 243
Østensen, R., Oreiro, R., Solheim, J.-E., et al. 2010, A&A, 513, A6
Østensen, R., Solheim, J.-E., Heber, U., et al. 2001, A&A, 368, 175
Østensen, R. H., & Van Winckel, H. 2012, in ASP Conf. Ser. 452, Fifth Meeting on Hot Subdwarf Stars and Related Objects, ed. D. Kilkenny, C. S. Jeffery, & C. Koen (San Francisco, CA: ASP), 163
Otani, T., Oswalt, T. D., Lynas-Gray, A. E., et al. 2018, ApJ, 859, 145
Paparo, M., Szeidl, B., & Mahdy, H. A. 1988, Ap&SS, 149, 73
Pelisoli, I., Neunteufel, S., Geier, S., et al. 2021, NatAs, 5, 1052
Pulley, D., Faillace, G., Smith, D., Watkins, A., & von Harrach, S. 2018, A&A, 611, A48
Randall, S. K., Van Grootel, V., Fontaine, G., Charpinet, S., & Brassard, P. 2009, A&A, 507, 911
Riello, M., De Angeli, F., Evans, D. W., et al. 2021, A&A, 649, A3
Saffer, R. A., Bergeron, P., Koester, D., & Liebert, J. 1994, ApJ, 432, 351
Schechter, P. L., Mateo, M., & Saha, A. 1993, PASP, 105, 1342
Schuh, S., Huber, J., Dreizler, S., et al. 2006, A&A, 445, 31
Seaton, M. J. 1979, MNRAS, 187, 73P
Shibahashi, H., & Kurtz, D. W. 2012, MNRAS, 422, 738
Shibahashi, H., Kurtz, D. W., & Murphy, S. 2015, MNRAS, 450, 3999
Silvotti, R., Østensen, R., & Telting, J. 2020, arXiv:2002.04545
Silvotti, R., Schaffenroth, V., Heber, U., et al. 2018, MNRAS, 500, 2461
Silvotti, R., Schuh, S., Janulis, R., et al. 2007, Natur, 449, 189
Silvotti, R., Schuh, S., Kim, S.-L., et al. 2018, A&A, 611, 85
Smart, W. M., & Green, R. M. 1977, Textbook on Spherical Astronomy (Cambridge: Cambridge Univ. Press)
Sterken, C. 2005, in ASP Conf. Ser. 335, The Light-Time Effect in Astrophysics, ed. C. Sterken (San Francisco, CA: ASP), 215
Stobie, R. S., Kilkenny, D., O'Donoghue, D., et al. 1997, MNRAS, 287, 848
Sullivan, D. J., Metcalfe, T. S., O'Donoghue, D., et al. 2008, MNRAS, 387, 137
Tauris, T. M., & van den Heuvel, E. P. J. 2006, in Compact Stellar X-ray Sources, ed. W. Lewin & M. van der Klis (Cambridge: Cambridge Univ. Press)
Telting, J. H., Baran, A. S., Nemeth, P., et al. 2014, A&A, 570, 129
Telting, J. H., Østensen, R. H., & Baran, A. S. 2012, A&A, 544, A1
Timothy, J. G. 1983, PASP, 95, 810
Toonen, S., Portegies Zwart, S., Hamers, A. S., & Bandopadhyay, D. 2020, A&A, 640, A16
Underhill, A. B. 1968, BAN, 19, 526
Vos, J., Boobrick, A., & Vučković, M. 2020, A&A, 641, A163
Vos, J., Németh, P., Vučković, M., Østensen, R., & Parsons, S. 2018, MNRAS, 473, 693
Vos, J., Vučković, M., Chen, X., et al. 2019a, MNRAS, 482, 4592
Vos, J., Vučković, M., Chen, X., et al. 2019b, CoSka, 49, 264

Wade, R., Barlow, B., Liss, S., & Stark, M. 2014, in ASP Conf. Ser. 481, 6th Meeting on Hot Subdwarf Stars and Related Objects, ed. V. Van Grootel et al. (San Francisco, CA: ASP), 311
Winget, D. E., & Kepler, S. O. 2008, ARA&A, 46, 157
Woltger, J., Jr. 1922, BAN, 1, 93
Wright, E. L., Eisenhardt, P. R. M., Mainzer, A. K., et al. 2010, AJ, 140, 1868
Wright, J. T., & Eastman, J. D. 2014, PASP, 126, 838
Wu, Y., Chen, X., Chen, H., Li, Z., & Han, Z. 2020, A&A, 634, A126
Wu, Y., Chen, X., Li, Z., & Han, Z. 2018, A&A, 618, A14
Xiong, H., Chen, X., Podsiadlowski, P., Li, Y., & Han, Z. 2017, A&A, 599, A54
Zong, W., Charpinet, S., Fu, J.-N., et al. 2018, ApJ, 853, 98
Zong, W., Charpinet, S., Vauclair, G., Giammichele, N., & Van Grootel, V. 2016, A&A, 585, A22